

Stable nanofacets in $[11\bar{1}]$ tilt grain boundaries of face-centered cubic metals

Tobias Brink,^{*} Lena Langenohl,[†] Swetha Pemma, Christian H. Liebscher, and Gerhard Dehm
Max-Planck-Institut für Eisenforschung GmbH, Max-Planck-Straße 1, 40237 Düsseldorf, Germany
 (Dated: April 23, 2024)

Grain boundaries can dissociate into facets if that reduces their excess energy. This, however, introduces line defects at the facet junctions, which present a driving force to grow the facets in order to reduce the total number of junctions and thus the system's energy. Often, micrometer-sized facet lengths are observed and facet growth only arrests for kinetic reasons. So far, energetically stable, finite-sized facets have not been observed, even though theoretical stability conditions have already been proposed. Here, we show a case where nanometer-sized facets are indeed stable compared to longer facets in $[11\bar{1}]$ tilt grain boundaries in Cu by atomistic simulation and transmission electron microscopy. The facet junctions lack a Burgers vector component, which is unusual, but which removes the main energy cost of facet junctions. Only attractive interactions via line forces remain, which result from a discontinuity of grain boundary excess stress at the junction. Atomistic simulations predict that the same phenomenon also occurs in at least Al and Ag.

I. INTRODUCTION

Grain boundaries (GBs) are planar defects in crystalline solids and thus lead to an excess (free) energy. Oftentimes, GBs nevertheless remain in the system for kinetic reasons, but tend to reduce their excess energy locally. For example, if the GB energy is sufficiently anisotropic, GBs are known to decompose into energetically favorable facets. Typically, asymmetric GBs split into symmetric facets [1, 2], but transitions from one symmetric GB plane into facets of different symmetric GB planes are also known, most famously for $\Sigma 3$ $[11\bar{1}]$ tilt GBs with $\{011\}$ habit planes in fcc metals [3–7]. Faceting/defaceting transitions as a function of temperature were reported [3, 6, 8]. However, once facets appear, there is a driving force for their growth [5, 6, 9]. This is because the line separating different facets—the facet junction—is a defect [10–12] and the system can reduce its energy by reducing the number of junctions [5, 6]. Nanoscale facet sizes have been observed [12, 13], but there the facet junctions are most likely kinetically pinned by immobile GB defects [12] or segregated elements [13].

Here, we report on more general $[11\bar{1}]$ tilt GBs in fcc metals. The $\Sigma 19b$ $[11\bar{1}]$ $\{178\}$ (misorientation $\theta = 46.83^\circ$) and $\Sigma 37c$ $[11\bar{1}]$ $\{11011\}$ GBs ($\theta = 50.57^\circ$) in Cu and Al are close to the $\Sigma 3$ $[11\bar{1}]$ $\{011\}$ GB ($\theta = 60^\circ$), but do not exhibit macroscopic faceting [14–16]. Instead, an ordered GB structure termed domino was found [14–17]. In Cu, an additional pearl structure occurs [14, 15, 17], meaning two GB phases [18–22] exist and can transition into one another based on the thermodynamic conditions [14, 15, 17]. On the second symmetric plane, inclined by 30° , only a single GB phase (termed zipper) was reported for $\Sigma 19b$ $[11\bar{1}]$ $\{235\}$ and $\Sigma 37c$ $[11\bar{1}]$ $\{347\}$ GBs [16, 23, 24]. Figure 1 shows these GB phases and the crystallography of the $\Sigma 37c$ GB as an example.

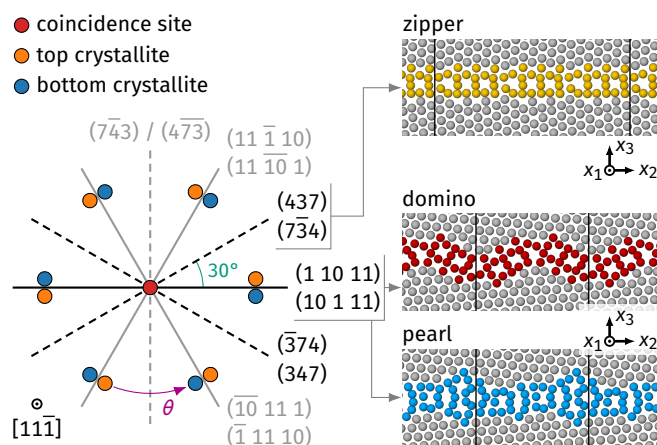


FIG. 1. Crystallography of $\Sigma 37c$ $[11\bar{1}]$ tilt GBs and their GB phases. An excerpt of the dichromatic pattern around a coincidence site shows the possible symmetric GB planes (lines): Solid lines exhibit the domino and pearl phases, while dashed lines exhibit the zipper phases, as shown in the snapshots on the right. Here, the pearl phase will not be discussed further, as it is not relevant for nanofaceting. For the GB habit planes, Miller indices are listed for the respective crystallographic planes of the top and bottom crystallite (in that order). Equivalent planes occur every 60° due to the three-fold symmetry of the fcc crystal. The two variants of symmetric planes are inclined by 30° . For simplicity, we concentrate on the GB planes in black and not on the crystallographically equivalent gray planes. Our convention for the simulation cell coordinate systems is $x_1 \parallel [11\bar{1}]$, x_2 lying in the GB plane, and x_3 being the GB plane normal. Axes x_2 and x_3 are different crystallographic directions for each GB (compare, e.g., zipper with domino). The other tilt GBs in this paper have equivalent crystallography for their respective misorientation θ .

In this paper, we will focus on the relation between the domino and zipper phases and will not discuss the pearl phase in detail: We demonstrate that the domino phase does in fact consist of zipper structure facets and that its facet junctions have an attractive interaction. This means that the domino phase's GB energy is lower for shorter facet lengths and that the observed nanofacets are energetically stable.

^{*} t.brink@mpie.de; T.B. and L.L. contributed equally.

[†] T.B. and L.L. contributed equally.

II. METHODS

A. Simulation

We used LAMMPS [25, 26] for molecular statics and molecular dynamics (MD) simulations of $[11\bar{1}]$ tilt GBs using embedded atom method (EAM) potentials for Cu [27], Al [28], and Ag [29]. Bicrystals were constructed by joining two crystallites in the desired orientation, sampling different relative displacements, and minimizing atomic positions with regards to the energy until the desired GB phases were found ($T = 0$ K). Details are provided in previous publications [17, 24]. GB planes and Σ values as function of the misorientation were found with the code from Ref. [30]. As a convention, we call the tilt axis direction x_1 , its normal along the (average) GB plane x_2 , and the GB plane normal x_3 .

We observed the evolution of GB facets using MD simulations with a time integration step of 2 fs. Temperature was controlled in the whole system with Nosé–Hoover thermostats. We used periodic boundary conditions along the tilt axis x_1 and open boundaries normal to the GB in x_3 direction. We also used periodic boundaries in x_2 direction where not specified otherwise. The simulation cell length in periodic directions was fixed according to the relevant fcc lattice constant at the target temperature. We visualized MD simulations with OVITO [31] and distinguished between fcc and GB atoms using the polyhedral template matching method [32].

Raw (meta-)data for the simulations are provided in the companion dataset [33].

B. Experiment

We additionally conducted experiments on Cu thin films that were epitaxially grown on $\langle 0001 \rangle$ Al_2O_3 wafers. The films were subsequently annealed for at least 1 h at 673 to 723 K [15, 24]. TEM lamellas containing GBs with different misorientation angles and GB planes were extracted using the focused Ga^+ ion beam of a Thermo Fisher Scientific Scios2HiVac dual-beam secondary electron microscope. They were then investigated in a FEI Titan Themis 80-300 (Thermo Fisher Scientific) scanning transmission electron microscope (STEM) at a voltage of 300 kV, beam currents of 70 to 80 pA, and a convergence angle of 17.8 mrad. A high-angle annular dark field (HAADF) STEM detector (Fisheye Instruments Model 3000) with a collection angle of 78 to 200 mrad was used for the registration of all images. The interested reader is referred to Refs. [15, 24] for more details on the experimental methods.

Raw (meta-)data for the experiments are provided in the companion dataset [33].

C. Dislocation-like defects on GBs and construction of Burgers circuits

To investigate the GB facet junctions—which are line defects—we first define how to calculate the Burgers vector content of GB defects. In general, a Burgers vector is a line integral over the elastic strain field as [34]

$$\mathbf{b} = \oint_C \frac{\partial \mathbf{u}}{\partial l} dl, \quad (1)$$

where C is a closed line around the defect of interest, \mathbf{u} is the elastic displacement field, and l is the integration variable along the line C . On a crystal lattice, this can be discretized by using $\mathbf{u} = \mathbf{x} - \mathbf{X}$, where \mathbf{x} are the actual atomic coordinates and \mathbf{X} the atomic coordinates in the defect-free reference system. If we do the integration from one atom to the next, using steps of $\Delta \mathbf{x}$ (with corresponding $\Delta \mathbf{X}$), we arrive at [34]

$$\mathbf{b} = \sum_{i \in C} \Delta \mathbf{X}_i. \quad (2)$$

For GB defects (e.g., disconnections/secondary GB dislocations), we simply define the reference coordinates \mathbf{X} in terms of a system that already contains the GB that we want to treat as defect free. As a consequence a defect is always defined in relation to a chosen reference system, which is useful when treating defects of defects, e.g. line defects of GBs. We here ignore the intrinsic (geometric) dislocation content of a specific GB and only ask how does the total dislocation content of a defective GB differ from what we define as a defect-free GB.

We utilize a simple method in the form used by Medlin et al. [12]. Here, the crystals abutting the GB are indexed and a closed loop around the GB defect is formed by going from atom to atom in steps of $\Delta \mathbf{X}$. In each of the two crystallites λ and μ , the steps $\Delta \mathbf{X}$ are summed up for a partial circuit that is fully contained in the GB-free parts of the respective crystallite. The closed line C should then only be missing two GB crossings, for which we cannot easily access \mathbf{X} . If these crossings are chosen at crystallographically equivalent sites, however, the sum of these two crossings equals $\mathbf{0}$ and they can be ignored for obtaining \mathbf{b} . Finally, the two crystal lattices are rotated towards each other [35], here around the tilt axis, as just adding up the two partial circuits would also contain the primary dislocation content of the GB (compare Read and Shockley’s equation [36]). Thus, the partial circuits $\sum_{i \in \lambda} \Delta \mathbf{X}_i$ and $\sum_{i \in \mu} \Delta \mathbf{X}_i$ are rotated into a common coordinate system before summing, thus obtaining only the additional Burgers vector content [12, 35]. Usually, we would use a rotation with the misorientation angle θ for the given tilt GB to perform this coordinate transformation. However, we can in principle also use the misorientation angle of another GB. This then allows us to locally extract the difference of Burgers vector content between different misorientations, e.g., to describe a $\Sigma 37c$ GB as a $\Sigma 3$ GB with defects.

For GB facet junctions, the two GB crossing cannot be made equivalent because both facets are rotated against each other [16]. For such cases, Frolov et al. proposed a method where $\Delta\mathbf{X}$ of the GB crossings are measured directly in a reference system that has to be simulated separately [37]. This is then added to the partial circuits from the previous method.

III. RESULTS

A. Stable nanofaceting

The $\Sigma 37c$ $[11\bar{1}] \{11011\}$ domino phase from atomistic simulations of Cu is shown in Fig. 2(a). Red lines highlight an arbitrary choice of atomic motifs—which we simply call “squares”—serving to guide the eye. It appears that the two motifs are each inclined by $\pm 30^\circ$ towards the GB plane, coinciding with the indicated crystal directions of the inset coordinate systems. They correspond to the habit planes of the zipper structure in the $\Sigma 37c$ $[11\bar{1}] \{347\}$ GB [Figs. 2(b)–(c)]. We can find the same square motifs from the domino phase in the zipper phase. By rotation of the zipper structures around $[11\bar{1}]$ by $\pm 30^\circ$, we can combine the zipper structures into the domino phase without introducing long-ranged lattice distortions (Fig. 3(a) and Supplemental Fig. S6 in Ref. [38]). The same is found for other misorientation angles we investigated ($\theta = 46.83^\circ$ to 55.59° , see Supplemental Figs. S1–S15). This suggests that the domino phase can be considered as a nanofaceted variant of the zipper structure. The structures in Al and Ag are the same [17] and this result consequently also applies to these metals. In previous experiments [14–16] and simulations [14, 15, 17], however, facet growth was never observed for domino. This is atypical, since—for example—the related $\Sigma 3$ $[11\bar{1}] \{011\}$ is prone to facet formation and growth (at least at low temperatures) [3–7, 16]. Consequently, it is possible that the domino phase is not faceted, but simply related to the zipper structure.

To clarify this, we investigated the GB energies when artificially constructing longer facets for different misorientation angles. Since the combination of two rotated zipper structures does not imply any additional strain and fits seamlessly at the joints, we can easily construct different facet lengths consisting of multiple zipper units. This allows to compute the GB energies

$$\gamma = \frac{E_{\text{GB}} - Ne_{\text{coh}}}{A} \quad (3)$$

for $T = 0$ and without externally-applied stress ($\sigma = 0$), with E_{GB} being the energy of a region consisting of N atoms containing the GB, and e_{coh} being the cohesive energy per atom of the bulk fcc phase (defined here as a negative number). The GB area A is the area projected onto the average GB plane, e.g., the (11011) plane in Fig. 2(a), even for faceted GBs. Figure 3(c) shows that the minimum GB energy always occurs at the smallest facet length for our samples with $46.83^\circ \leq \theta \leq 55.59^\circ$,

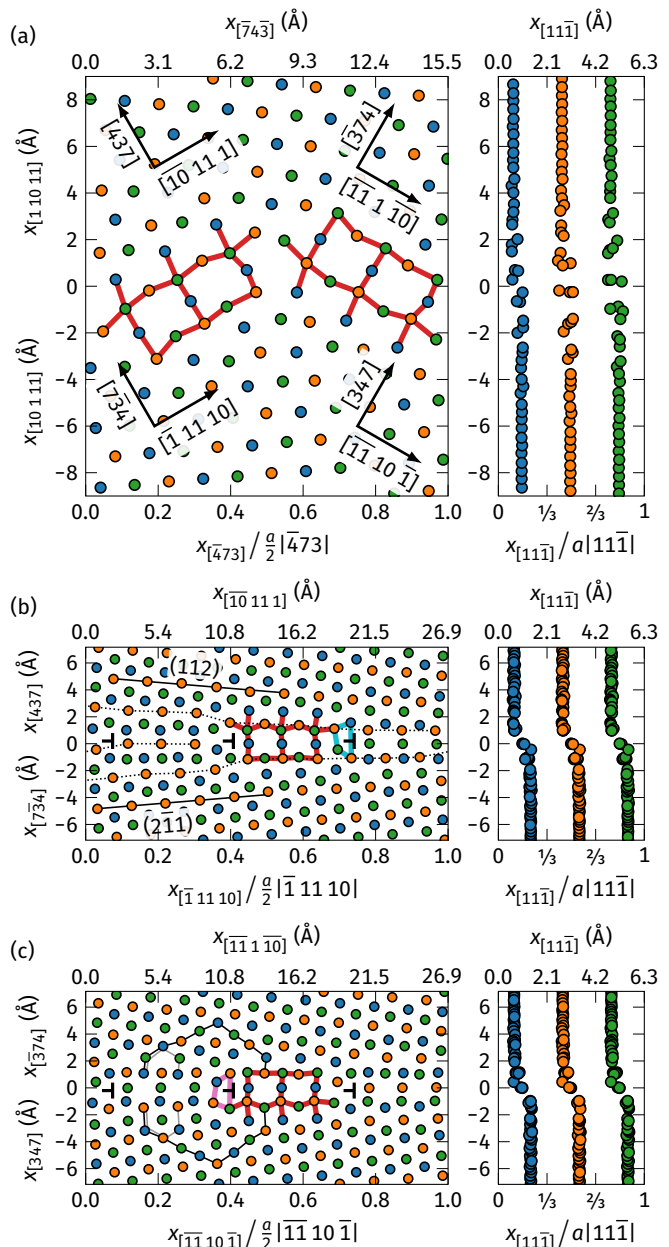


FIG. 2. Motifs of $\Sigma 37c$ GBs in Cu. (a) Domino consists of a (b) left and (c) right zipper motif. Atom color indicates ABC stacking. Red lines are used to highlight the square motifs, blue and pink lines each highlight one trapezoidal unit. Black lines in (b) follow $\{112\}$ planes, which is the GB plane of the corresponding $\Sigma 3$ GB, while black/gray lines in (c) indicate Burgers circuits. As discussed in Sec. II C, the local dislocation content with reference to the $\Sigma 3$ $[11\bar{1}] \{112\}$ GB can be obtained using a modification of the method employed by Medlin et al. [12]. We obtain $\mathbf{b} = a/6\langle 112 \rangle$ for the black circuit and $\mathbf{0}$ for the gray one, indicating that the trapezoidal motif has dislocation character. Some more technical details are provided in Supplemental Fig. S23.

opposite to the effects observed in many other faceted GBs [5–7] and in our $\Sigma 3$ GB [$\theta = 60^\circ$, dark gray line

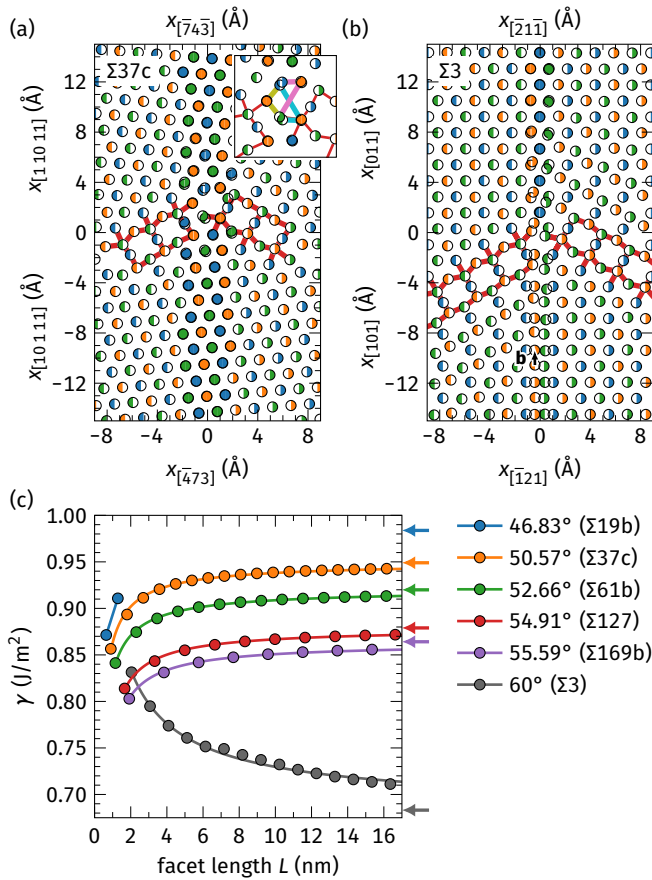


FIG. 3. Facets in Cu. (a) Joining two $\Sigma 37c$ zippers without further relaxation. The atoms coming from the left zipper are indicated by circles filled on the left half and vice versa for the right zipper. In the center region, atoms from both structures are shown and overlap. Thus there is no Burgers vector. The inset shows how the trapezoidal units indicated in Fig. 2 overlap seamlessly. The yellow lines are shared between both trapezoidal units. (b) For $\Sigma 3$, however, the indicated Burgers vector remains, here seen as a shift in the bottom crystal. (c) GB energies of GBs with an average plane corresponding to domino but with different facet lengths L . The arrows indicate the GB energy of the zipper phase projected onto the domino GB plane (first term of Eq. 4). This corresponds to infinite facet lengths. For $\Sigma 19b$, longer facets became unstable even in static minimization, reverting partially to domino and are not shown here.

in Fig. 3(c)]. In fact, energies converge asymptotically to the value of zipper facets with zero junction energy (infinite facet length), showing that nanofacets are even stable compared to microscale facets. The same results are obtained for Al and Ag (Supplemental Fig. S17). As a further verification step, we also conducted an MD simulation starting from longer facets consisting of 11 zipper motifs and thus a facet length of $L = 9.9$ nm. In the periodic tilt axis direction we used a thickness of 6.3 nm. The simulation was performed at 500 K, to provide just enough thermal energy that the system can evolve in the limited timescale of MD, while not probing the high-

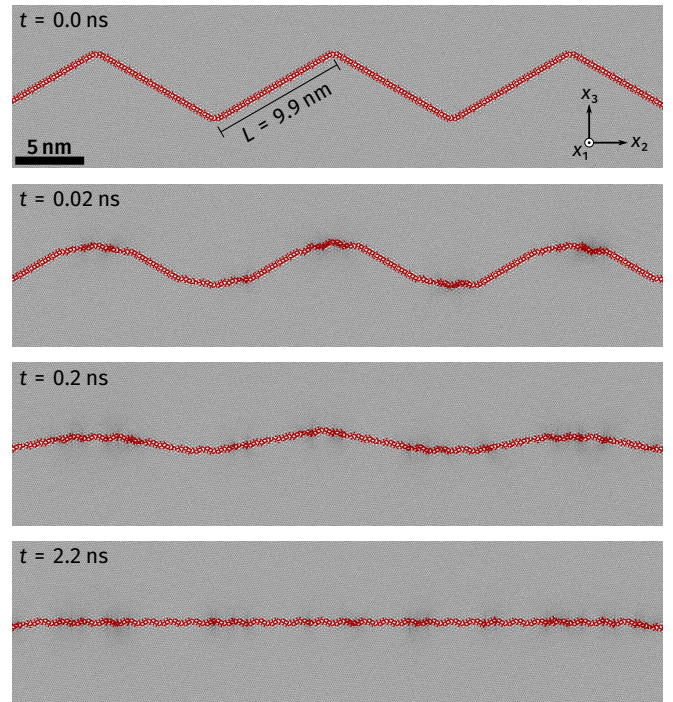


FIG. 4. MD simulation of a $\Sigma 37c$ GB with initial facet length of $L = 9.9$ nm at $T = 500$ K. Gray atoms were identified by polyhedral template matching as fcc atoms, while red atoms represent non-fcc atoms, i.e., the GB. The facets almost immediately start shrinking at the junction. This also indicates that even macroscopic facets would be able to shrink to nanofacets, because the process starts on the nanoscale at the junctions—where nanofaceting can immediately reduce the GB energy—and then proceeds along the GB.

temperature regime. The facet junctions of this system immediately serve as nucleation sites for the appearance of nanofacets with minimal facet length (Fig. 4). The GB is fully nanofaceted after 2.2 ns. Apart from confirming the hypothesis that the domino phase can be regarded as a stable, nanofaceted zipper variant, this also demonstrates that even a GB with micrometer-sized facets would be unstable against facet length reduction, because the facet refinement starts locally at the junctions. It remains to explore why this phenomenon occurs in our $[11\bar{1}]$ tilt GBs for $\theta < 60^\circ$.

B. Model

In Eq. 5 of Ref. [5], a criterion was derived for energetic stabilization of finite facet lengths from interactions between dislocation content and line forces at the junctions. The facet junction energy consists of contributions from the junction's core energy, dislocation interaction (due to the junction Burgers vector \mathbf{b}), and line forces f due to a discontinuity of the GB excess stress $[\tau]$ at the junction. We can thus slightly restate the energy of faceted GBs

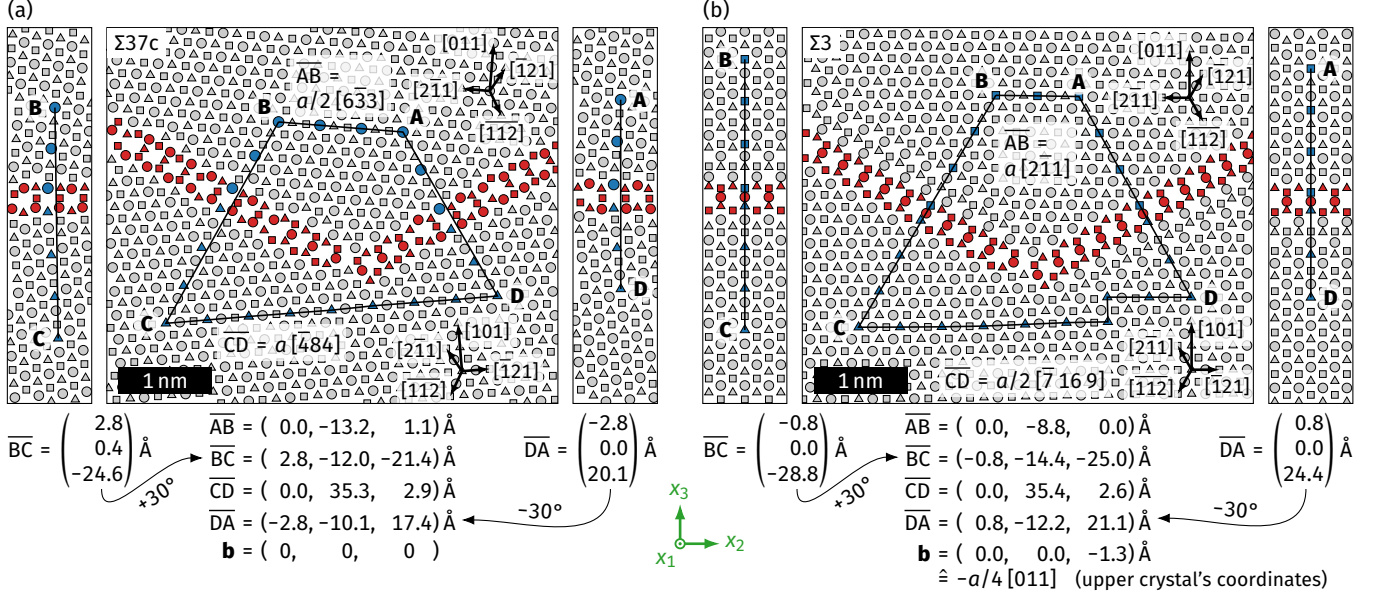


FIG. 5. Burgers circuits around facet junctions in the (a) $\Sigma 37c$ and (b) $\Sigma 3$ tilt GBs. Red atoms highlight the GB motifs. The symbols used for the atoms (circle, triangle, square) indicate that they belong to different $(11\bar{1})$ planes. Blue atoms and black lines represent the closed Burgers circuit. The circuits are constructed as explained in the methods section: After indexing the crystallites, the lines \overline{AB} and \overline{CD} are constructed by following the interatomic distances $\Delta \mathbf{X}$ in the defect-free reference crystal along the indexed crystal directions; \overline{AB} in the coordinate system of the top crystal and \overline{CD} in the coordinate system of the bottom crystal. They are then transformed into the common coordinate system (x_1, x_2, x_3) as shown below the images in green. Values are listed in Å below the images. The lines \overline{BC} and \overline{DA} are then marked in the system containing the facet junction and transposed into the junction-free systems containing only the left or right zipper structure (smaller images on the left and right). The line vectors are measured directly in these simulations from the atomic positions of points A, B, C, and D. The results are then rotated by $\pm 30^\circ$ around x_1 . We then obtain $\mathbf{b} = \overline{ABCD}$, which is (a) $\mathbf{b} = \mathbf{0}$ for the $\Sigma 37c$ GB and (b) $\mathbf{b} = a/4[0\bar{1}1]$ for the $\Sigma 3$ GB. As expected, the Burgers vector of the other facet junction in $\Sigma 3$ has the opposite sign ($a/4[011]$, analysis in Supplemental Fig. S18).

from Ref. [5] as

$$\gamma = \frac{\gamma_{\text{facet}}}{\cos \phi} + \frac{E_{\text{core}}}{tL} + (k_1 b^2 + k_2 f b - k_3 f^2) \frac{\ln(L/\delta_0)}{L}. \quad (4)$$

The first term is the GB energy of the facet's GB phase projected onto the average GB plane, where ϕ is the inclination of the facet (here $\phi = 30^\circ$, generally in the range $[0^\circ; 90^\circ]$). The second term contains the facet junction's core energy E_{core} , normalized by the facet junction line length t along the tilt axis and the facet length L (distance of junctions). The final term includes the dislocation-dislocation interactions ($\propto b^2$), interactions between line forces ($\propto f^2$), and interactions between dislocations and line forces ($\propto f b$). The prefactors $k_i > 0$ contain elastic constants of the material [34, 39–41]. The length $\delta_0 \ll L$ is the core size of the facet junction. A more detailed derivation (for GB phase junctions instead of facet junctions, but mathematically equivalent) can be found, e.g., in Ref. [42], but is not required here.

Some clarification is, however, helpful to understand the implications of this model. The two final terms are equivalent to the energy of a low-angle GB (array of dislocations), except for the addition of the line force f [43, 44]. In the typical derivation, the energy of a low-angle GB

can be calculated under the assumption that edge dislocations are arranged such that their compressive and tensile strain fields overlap. This is the same as the interaction of two parallel dislocations with opposite Burgers vectors, which means that the strain energy per dislocation only has to be calculated within a radius corresponding to the dislocation distance, because it cancels out beyond that range [43]. In other words, dislocations introduce strain energy, but that strain energy can be reduced (but not eliminated) by interaction with a nearby dislocation with opposite Burgers vector [43]. The reduction is greater the closer the dislocations are (more overlap of their opposite displacement fields). Facet junctions also have to have alternating Burgers vectors to preserve the total dislocation content of the GB. They can therefore be treated the same way due to their alternating strain fields [5]. This means that while junction Burgers vectors have an attractive force, each Burgers vector leads to a net energy increase ($k_1 b^2 \geq 0$). An increase of the facet length L would therefore always lower the total number of facet junctions and thus the total energy. GBs intrinsically also have a strain energy cost due to their excess stress. If there is a discontinuity of this excess stress at the facet junctions, the overlapping GB strain fields partially com-

TABLE I. GB energy γ and excess stress $[\tau_{ij}]$ for $\Sigma 37c$ and $\Sigma 3$ GBs in Cu. The left and right zipper are degenerate states, as evidenced by their equal GB energy, but they can differ in the sign of their excess shear stress $[\tau_{12}]$. Data for more misorientations, as well as for Al and Ag can be found in Supplemental Tables S-I and S-II and Supplemental Figs. S20–S21.

| structure | γ (J/m ²) | $[\tau_{11}]$ (J/m ²) | $[\tau_{22}]$ (J/m ²) | $[\tau_{12}]$ (J/m ²) |
|------------------------|---------------------------------|--------------------------------------|--------------------------------------|--------------------------------------|
| $\Sigma 37c$ domino | 0.857 | -0.18 | +0.24 | 0.00 |
| left zipper | 0.822 | +0.19 | -0.37 | +0.15 |
| right zipper | 0.822 | +0.19 | -0.37 | -0.15 |
| $\Sigma 3$ left zipper | 0.592 | -2.28 | -0.57 | 0.00 |
| right zipper | 0.592 | -2.28 | -0.57 | 0.00 |

pensate each other and the GB's strain energy is reduced. This can be expressed as line forces that are opposite at each junction, lowering the total energy ($k_3 f^2 \leq 0$). More detailed derivations have been provided for surface phase boundaries that also exhibit such line forces [45]. The interaction $k_2 f b$ does not play a role in our specific case, as shown below.

Stabilization of nanofacets is thus a matter of competition between these terms. Equation 4 has an extremum at length $L = e\delta_0 \approx 0$ (due to $\delta_0 \ll L$). It is a minimum if the prefactor of the final term is negative [46], i.e., if

$$f > b \frac{k_2 + \sqrt{k_2^2 + 4k_1 k_3}}{2k_3}. \quad (5)$$

Fulfilling this condition thus means that facet growth is predicted to be disabled. A Burgers circuit around a junction in our faceted $\Sigma 37c$ GB reveals that the Burgers vector content of the junction with reference to the zipper phase is zero [Fig. 5(a)]. This is consistent with the combination of left and right zipper leading to an undistorted domino phase motif [Fig. 3(a)] and is true for all of our GBs with $\theta < 60^\circ$. Facet junctions in $\Sigma 3$ GBs, in contrast, contain a finite dislocation content [Fig. 3(b) and Fig. 5(b)]. To fulfill the criterion from Ref. [5] for $b = 0$, we just need a positive f . In the next step, we will therefore estimate f for our GBs.

We describe the GB excess stress as a tensorial value, defined at $T = 0$ and $\sigma = 0$ as

$$[\tau_{ij}] = \frac{\bar{\sigma}_{ij} V}{A}, \quad (6)$$

where $\bar{\sigma}_{ij}$ is the average residual stress in a region of volume V around the GB [47, 48]. Indices $i, j = 1$ correspond to the tilt axis, $i, j = 2$ to its orthogonal direction in the GB plane, and $i, j = 3$ to the GB normal. Excess stresses of $\Sigma 37c$ and $\Sigma 3$ GBs are listed in Table I. Notably, the excess shear stresses $[\tau_{12}]$ for the two zipper structures that make up the domino structures have opposite values for all $\theta < 60^\circ$ (e.g., ± 0.15 J/m² for $\Sigma 37c$ in Cu), while all other components are the same. This can also be visualized by computing the lattice strains (per-atom strain

with reference to the perfect fcc lattice) as calculated by the polyhedral template matching method [32] in OVITO [31]: The shear strains E_{12} alternate between the facets (Supplemental Fig. S19).

The line forces can be computed as the sum of the two stress vectors of the zipper facets. These vectors are calculated at an (imaginary) surface separating the facets at a junction. This surface plane must therefore be orthogonal to the average GB plane and have a normal vector $\mathbf{v} = (0, 1, 0)$, representing the x_2 direction along the GB (e.g., $[\bar{4}73]$ in the coordinate system of the lower crystallite of the $\Sigma 37c$ domino GB) [42, 49]. Using Einstein notation we obtain

$$f_j = \pm [\tau_{ij}^{\text{left}}] \cdot v_i \mp [\tau_{ij}^{\text{right}}] \cdot v_i. \quad (7)$$

The two stress vectors at the separating plane point by definition in opposite directions (analogous to action/reaction forces), leading to opposite signs for the left and right junction terms. The overall sign of the expression depends on the specific junction. Due to the opposite sign of $[\tau_{12}]$ in both facets, this yields a nonzero value of f_1 with alternating signs at each junction [50]. The line force thus contributes an energy proportional to $-f_1^2 \ln(L/\delta_0)$ per junction, where L is the facet length [42, 49]. As stated above, this is a result of the reduction of GB strain energy due to the alternating signs of the excess shear stress. In other words, in our case there is no Burgers vector but only opposite and therefore attractive line forces at the junctions and the criterion for facet shrinkage is trivially fulfilled. This is true for all of our GBs with misorientations $\theta < 60^\circ$. Similar formalisms have been used for surface phase coexistence [45, 51–53]. For the $\Sigma 3$ GB, we find in contrast $[\tau_{12}] = 0$ and $\mathbf{b} \neq \mathbf{0}$, leading to a repulsion of the junctions and facet growth. The lines in Fig. 3(c) are fits of Eq. 4 to the simulated GB energies, showing the applicability of the model.

C. Zipper structure and facet lengths

Regarding the zipper structure, the motifs in the $\Sigma 3$ $\{112\}$ GB and close-by GBs with lower misorientation angles θ are similar [Fig. 7(f)–(g) and Supplemental Figs. S2, S5, S8, S11, S14, S16]: All GBs contain the squares indicated in red. Additionally, GBs with $\theta < 60^\circ$ contain another motif, indicated by the edge dislocation symbol in Fig. 2(b)–(c). We call this the trapezoidal unit [24]. Inspection of the $\{112\}$ planes in Fig. 2(b) reveals that these motifs do indeed resemble edge dislocations: It appears that $\{112\}$ planes terminate at the trapezoidal unit. An analysis of the local stress fields [Fig. 6(a)] and a Burgers circuit analysis [Fig. 2(c)] confirm that these units can be regarded as virtual $a/6\langle 112 \rangle$ dislocations when compared to the reference state of the $\Sigma 3$ GB [24]. It is important to note that these are not real dislocations (in principle the primary dislocation content required to obtain a misorientation $\theta = 50.57^\circ$ for $\Sigma 37c$ is lower than to obtain $\theta = 60^\circ$ for $\Sigma 3$ [36]), but that they behave similarly. We

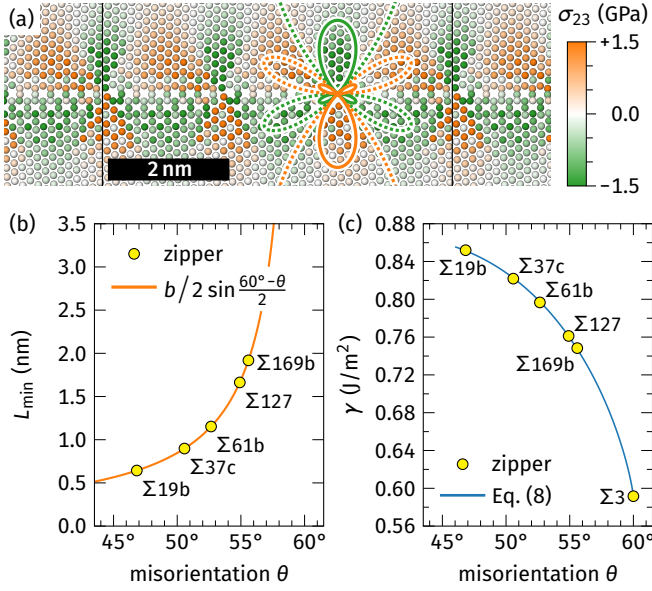


FIG. 6. The trapezoidal unit as a virtual dislocation in the zipper structures with $\theta < 60^\circ$. If the trapezoidal unit has the character of an edge dislocation, the shear stress component σ_{23} should be nonzero. The subfigure (a) shows the atomic stress of the zipper structure in the $\Sigma 169b$ tilt GB ($\theta = 55.59^\circ$), where the stress fields are most easily visualized. We also plotted the contour lines of the analytical solution of the shear stress for an $a/6\langle 112 \rangle$ edge dislocation [54]. The dashed lines represent $\sigma_{23} = \pm 0.25$ GPa and the solid lines ± 1 GPa. The analytical solution fits to the observed stress (more stress components and an analysis of the $\Sigma 3$ tilt GB are shown Supplemental Fig. S22). (b) Since the trapezoidal units have a Burgers vector (see also Supplemental Fig. S23), they compensate the difference in misorientation compared to the $\Sigma 3$ GB ($\theta = 60^\circ$) and their distance can be calculated via a reversal of the Read–Shockley equation (Eq. 9). (c) The GB energy of the zipper can consequently be decomposed into the GB energy of $\Sigma 3$ plus the energy of a low-angle GB (Eq. 8, see Supplemental Fig. S24 for additional data on Al and Ag).

thus term them “virtual dislocations”. The energy of the zipper GB can therefore be written as a combination of the $\Sigma 3$ GB energy plus the energy of a low-angle GB as

$$\gamma(\theta) = \gamma_{\Sigma 3} + \frac{Kb^2}{L_{\min}(\theta)} \ln \frac{L_{\min}(\theta)}{\pi\delta_0}, \quad (8)$$

where the second term is the energy of a low-angle GB [43, 44], defined by its dislocation interaction energy [43] with K being an elastic constant [$K = G/(4\pi - 4\pi\nu)$ for edge dislocations in isotropic materials with shear modulus G and Poisson’s ratio ν] and δ_0 an effective dislocation core size that also includes the core energy term [55, 56]. The length L_{\min} represents the distance between trapezoidal units.

This is relevant to the faceting because the distance between trapezoidal units can be written as

$$L_{\min}(\theta) = \frac{b}{2 \sin \frac{60^\circ - \theta}{2}} \quad (9)$$

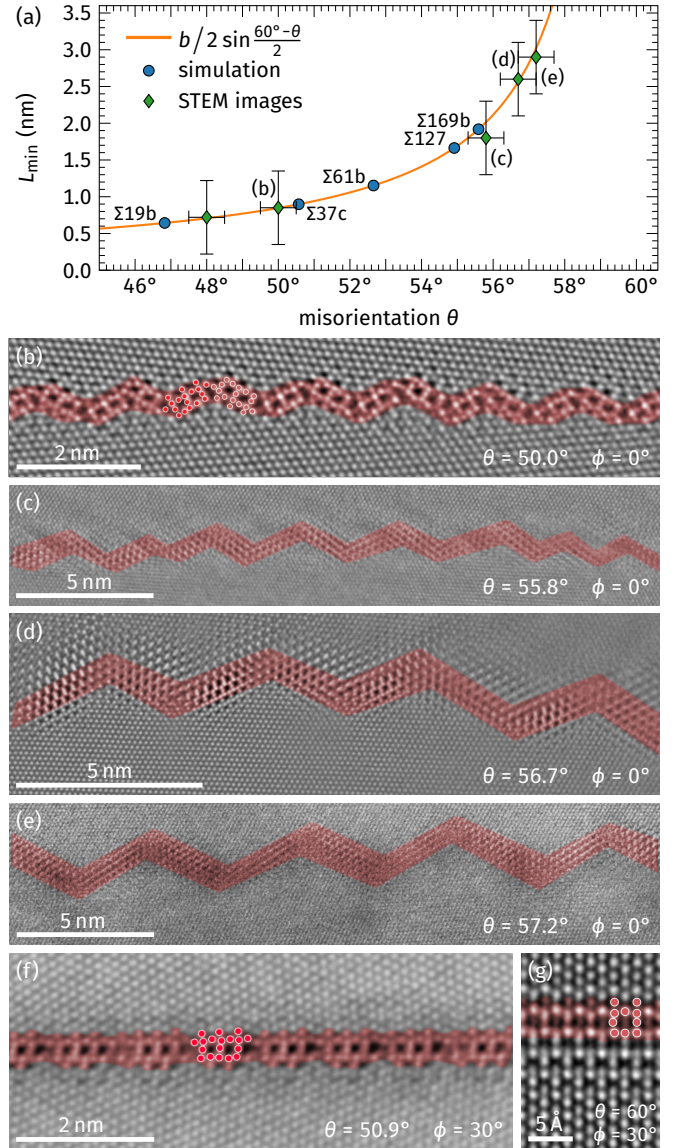


FIG. 7. (a) Predicted facet lengths in domino assuming that the zippers are joined at the trapezoidal unit and that the trapezoidal unit is a virtual dislocation with $\mathbf{b} = a/6\langle 112 \rangle$. Simulations represent the relevant domino phase, constructed by joining the left and right zipper structures. Experimental misorientations θ and facet lengths L are measured from the STEM images in (b)–(e) and from Fig. 1 in Ref. [14] for $\Sigma 19b$. Note that the GB in (d) is likely not edge-on and therefore appears much wider than the other GBs. Data in (b) is adapted from Ref. [15] and data in (f) and (g) is adapted from Ref. [24] under the terms of the Creative Commons Attribution 4.0 International license. The measurement error of θ in all experimental images is $\pm 0.5^\circ$.

via a reversal of Read and Shockley’s equation [36], as validated in Fig. 6(b). The GB energy from Eq. 8 with K and δ_0 as fit parameters then also matches the computed GB energies [Fig. 6(c)]. Figure 3(a)–(b) shows that the zipper facets join seamlessly at the trapezoidal unit, and cannot join seamlessly if it is absent ($\Sigma 3$). Thus, L_{\min}

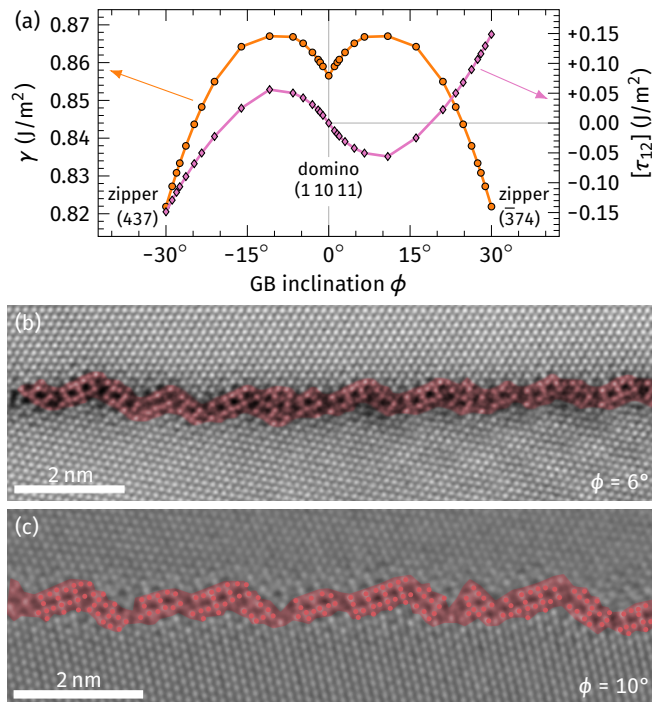


FIG. 8. (a) Changing inclination for the Σ_{37c} GB from the left zipper via domino to the right zipper by changing the length of one side of the facets. Inclination angle ϕ is relative to the domino plane. (b)–(c) STEM images of asymmetric Σ_{37c} GBs. The measured inclination angle has an uncertainty of $\pm 0.5^\circ$.

is also the minimal facet length of the domino structure, as confirmed in Fig. 7(a). Figures 7(b)–(e) show STEM images of domino phases with different misorientation angles θ . The simulations match the experimental observations where comparison is possible. For larger θ values it becomes obvious that the domino structure is faceted. The experimental facet lengths correspond to the predictions [Fig. 7(a)]. We never observed longer facets in our data, despite annealing after deposition for at least 1 h at around $T \approx 700 \text{ K} \sim 0.5T_{\text{melt}}$. Faceting/defaceting transitions in $\Sigma 3 \{011\}$ GBs in Al were previously observed on the micrometer scale over holding times of 40 min at similar homologous temperatures [3], showing that the facet-growth kinetics should definitely be sufficiently fast to observe nanofacet growth if there were an energetic driving force. The absence of long facets at atomic resolution in our experiment thus provides proof for the stabilization of nanofacets.

D. Asymmetric GBs

Combination of zipper structures into domino structures allows for a simple method to produce asymmetric GBs in between the zipper and domino inclinations by increasing the length of one of the facets. We constructed different inclinations ϕ for Σ_{37c} GBs and calculated their GB energies and excess properties using molecular statics.

Figure 8(a) shows that it is thus possible to gradually transition from domino to zipper and vice versa by changing the GB plane inclination. The combination of zipper structures with opposite values of $[\tau_{12}]$ into domino with $[\tau_{12}] = 0$ is also evident. We repeated these simulations for Al and Ag, yielding equivalent results (Supplemental Fig. S17). The energy landscape suggests that domino and zipper can in principle transition into each other.

For this, we performed two sets of MD simulations on Σ_{37c} tilt GBs in Al. We chose Al as an element because the pearl phase is not stable below 600 K [17] and we can thus avoid a GB phase transition into the pearl phase, which might suppress any inclination change. First, we build a simulation cell where the horizontal plane (with normal x_3) corresponds to the GB plane of the domino phase, shown in Fig. 9(a). We inserted a zipper GB (which was consequently inclined by 30° towards the domino plane) and used open boundary conditions in the x_2 direction, allowing the GB to rotate and thereby change its length. While the GB energy of domino is higher than that of zipper [Fig. 8(a)], the rotation onto the horizontal plane shortens the GB. Indeed, we observed that the system reduced its total energy by transforming into the domino phase, rotating by -30° . Second, we produced a cylindrical sample, such that all inclinations lead to the same GB length and fixed the GB in the center [Fig. 9(b)]. Thus, the GB can rotate but cannot change its length or migrate. Here, GBs with different inclinations slowly rotated towards the zipper structure/inclination, which has the lowest GB energy per unit area. This shows that inclination transitions are possible, but depend strongly on the boundary conditions and are significantly more complicated in realistic microstructures.

The fact that the nanofacets simultaneously act as pure steps on the GB ($\mathbf{b} = \mathbf{0}$) and allow the construction of asymmetric GBs raises the question of nomenclature. Indeed, GB facets are typically much larger than the structures observed here, although nanosized GB facets have been reported before [12, 13]. Instead of using the concept of faceting, one could therefore also consider the alternating facets as GB steps, especially on the asymmetric GBs, or even call the domino structure a reconstruction in analogy to surface science. We decided to call the phenomenon faceting nonetheless because the domino motifs are clearly two inclined zipper motifs and the construction of asymmetric GBs by faceting is well established. It seems arbitrary to us to draw a line between faceting and reconstruction on the basis of the facet length, although the stability of our nanofacets might provide a distinction.

Finally, other types of structural defects could also potentially compensate asymmetric inclinations and we do not claim that lengthening facets is the only way to construct asymmetric domino/zipper GBs. Nevertheless, Figs. 8(b)–(c) show STEM images of two different inclinations whose atomic structures indeed consist of longer and shorter facets, highlighting that low-energy configurations do occur this way.

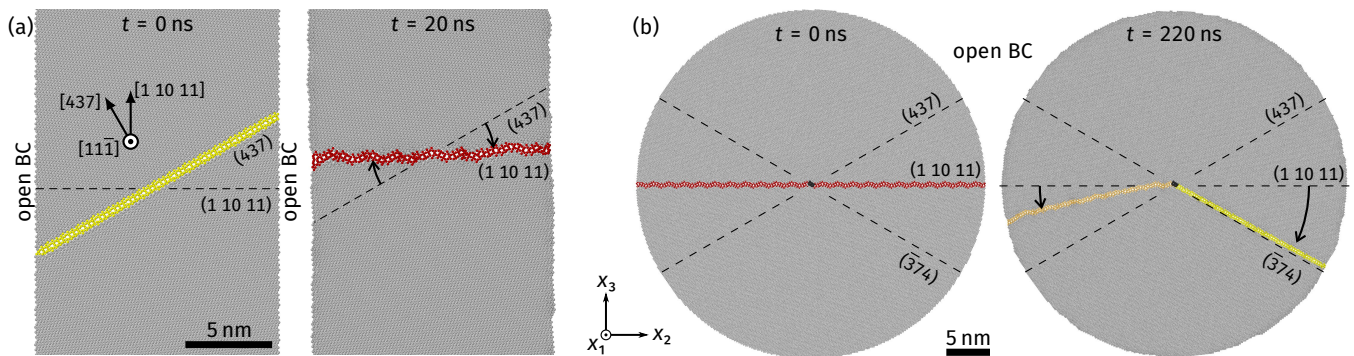


FIG. 9. MD simulations of inclination changes driven by the GB energy. Annealing was performed at $T = 600$ K, with subsequent cooling ($\dot{T} = 10^{11}$ K/s) to 100 K. We used $\Sigma 37c$ GBs in Al, which do not show any transition to the pearl phase in this temperature range in contrast to Cu [17]. Thickness along the periodic x_1 direction was 1.4 nm. The small thickness was chosen to accelerate the kinetics of inclination changes. (a) When starting from a zipper GB (yellow) inclined by 30° in a simulation cell with open boundary conditions in x_2 direction (left image), the GB can reduce its energy by rotating onto the (1 10 11) plane of the domino phase (red atoms, right image), despite the higher GB energy of domino compared to zipper. The reduction of GB area outweighs the normalized GB energy differences. (b) We then performed simulations where the GB area does not change with the inclination by using a cylindrical setup. The spatial positions of the GB atoms in the center of the cylinder (black) were fixed to only allow GB rotation, but not movement normal to its plane. Now the GB is driven from the initial domino phase (red atoms, left image) to the zipper phase (yellow atoms, right image), purely due to the differences in GB energy. However, even after 220 ns annealing time, the rotation on the left side is incomplete (orange atoms). This highlights that the small GB energy differences lead to small driving forces for rotation and generally relatively slow kinetics. These simulations demonstrate that inclination changes can be driven by GB energy but are highly dependent on the boundary conditions.

IV. CONCLUSION

A set of $[11\bar{1}]$ tilt GBs in fcc metals exhibit nanofacets that are energetically stable compared to longer facets at misorientations $\theta < 60^\circ$. We call the atomic structure of these GBs the domino structure. Atomic-resolution imaging is required to resolve the nanofacets experimentally. The GBs are made of zipper-type facets that can be joined seamlessly into domino structures (Fig. 2). Their facet junction occurs at the site of the zipper structure's trapezoidal motif—which behaves like an $a/6\langle 112 \rangle$ edge dislocation. The special feature of this motif is that it allows facets to join without introducing an additional facet junction Burgers vector. Only an attractive line force due to the GB excess stress remains (Eqs. 4–7). In agreement with theory [5], this is sufficient to stabilize the nanofacets energetically (Fig. 3). STEM experiments on Cu thin films confirm the predicted, nanoscale facet lengths for a range of misorientations (Fig. 7). Because the trapezoidal unit is not present in the more well-studied $\Sigma 3$ GBs, these GBs exhibit a junction Burgers vector and thus a driving force for facet growth. The faceting/defaceting in $\Sigma 3$ [3, 6, 8] is thus likely a sign of a GB phase transition (change

away from the domino/zipper structures) and should be investigated in the future.

ACKNOWLEDGMENTS

We thank Gunther Richter and his team from the Max Planck Institute for Intelligent Systems for producing the Cu thin film by molecular beam epitaxy. This project has received funding from the European Research Council (ERC) under the European Union's Horizon 2020 research and innovation programme (Grant agreement No. 787446; GB-CORRELATE).

T.B., G.D., and C.H.L. each conceptualized parts of the study. T.B. performed and analyzed the atomistic computer simulations, while S.P. analyzed the elastic interactions due to Burgers vectors. L.L. performed the experimental sample preparation, HAADF-STEM investigations, and analysis of the corresponding datasets. The project was supervised by C.H.L. and G.D., who also contributed to discussions. G.D. secured funding for T.B., L.L., and S.P. via the ERC grant GB-CORRELATE. T.B. and L.L. prepared the initial manuscript draft and all authors contributed to the preparation of the final manuscript.

[1] W. R. Wagner, T. Y. Tan, and R. W. Balluffi, Faceting of high-angle grain boundaries in the coincidence lattice, *Philos. Mag.* **29**, 895 (1974).

[2] A. Brokman, P. Bristowe, and R. Balluffi, Atomistic faceting of asymmetric tilt boundaries, *Scripta Metallurgica* **15**, 201 (1981).

- [3] T. E. Hsieh and R. W. Balluffi, Observations of roughening/de-faceting phase transitions in grain boundaries, *Acta Metallurgica* **37**, 2133 (1989).
- [4] B. B. Straumal, S. A. Polyakov, E. Bischoff, W. Gust, and E. J. Mittemeijer, Faceting of $\Sigma 3$ and $\Sigma 9$ grain boundaries in copper, *Interface Science* **2001** 9:3 **9**, 287 (2001).
- [5] J. C. Hamilton, D. J. Siegel, I. Daruka, and F. Léonard, Why do grain boundaries exhibit finite facet lengths?, *Phys. Rev. Lett.* **90**, 246102 (2003).
- [6] Z. X. Wu, Y. W. Zhang, and D. J. Srolovitz, Grain boundary finite length faceting, *Acta Mater.* **57**, 4278 (2009).
- [7] A. D. Banadaki and S. Patala, A simple faceting model for the interfacial and cleavage energies of $\Sigma 3$ grain boundaries in the complete boundary plane orientation space, *Comput. Mater. Sci.* **112**, 147 (2016).
- [8] B. B. Straumal, O. A. Kogtenkova, A. S. Gornakova, V. G. Sursaeva, and B. Baretzky, Review: grain boundary faceting–roughening phenomena, *Journal of Materials Science* **2015** 51:1 **51**, 382 (2016).
- [9] R. Hadian, B. Grabowski, M. W. Finnis, and J. Neugebauer, Migration mechanisms of a faceted grain boundary, *Phys. Rev. Mater.* **2**, 043601 (2018).
- [10] G. P. Dimitrakopoulos, T. H. Karakostas, and R. C. Pond, The defect character of interface junction lines, *Interface Sci.* **4**, 129 (1997).
- [11] R. C. Pond and V. Vitek, Periodic grain boundary structures in aluminium I. A combined experimental and theoretical investigation of coincidence grain boundary structure in aluminium, *Proc. R. Soc. Lond. A* **357**, 453 (1997).
- [12] D. L. Medlin, K. Hattar, J. A. Zimmerman, F. Abdeljawad, and S. M. Foiles, Defect character at grain boundary facet junctions: Analysis of an asymmetric $\Sigma = 5$ grain boundary in Fe, *Acta Mater.* **124**, 383 (2017).
- [13] N. J. Peter, T. Frolov, M. J. Duarte, R. Hadian, C. Ophus, C. Kirchlechner, C. H. Liebscher, and G. Dehm, Segregation-induced nanofaceting transition at an asymmetric tilt grain boundary in copper, *Phys. Rev. Lett.* **121**, 255502 (2018).
- [14] T. Meiners, T. Frolov, R. E. Rudd, G. Dehm, and C. H. Liebscher, Observations of grain-boundary phase transformations in an elemental metal, *Nature* **579**, 375 (2020).
- [15] L. Langenohl, T. Brink, R. Freitas, T. Frolov, G. Dehm, and C. H. Liebscher, Dual phase patterning during a congruent grain boundary phase transition in elemental copper, *Nat. Commun.* **13**, 3331 (2022).
- [16] S. Ahmad, T. Brink, C. H. Liebscher, and G. Dehm, Influence of variation in grain boundary parameters on the evolution of atomic structure and properties of [111] tilt boundaries in aluminum, *Acta Mater.* **268**, 119732 (2024).
- [17] T. Brink, L. Langenohl, H. Bishara, and G. Dehm, Universality of grain boundary phases in fcc metals: Case study on high-angle [111] symmetric tilt grain boundaries, *Phys. Rev. B* **107**, 054103 (2023).
- [18] E. W. Hart, Two-dimensional phase transformation in grain boundaries, *Scr. Metall.* **2**, 179 (1968).
- [19] W. Cahn, J., Transitions and phase equilibria among grain boundary structures, *J. Phys. Colloques* **43**, C6 (1982).
- [20] C. Rottman, Theory of phase transitions at internal interfaces, *J. Phys. Colloques* **49**, C5 (1988).
- [21] T. Frolov and Y. Mishin, Phases, phase equilibria, and phase rules in low-dimensional systems, *J. Chem. Phys.* **143**, 044706 (2015).
- [22] P. R. Cantwell, T. Frolov, T. J. Rupert, A. R. Krause, C. J. Marvel, G. S. Rohrer, J. M. Rickman, and M. P. Harmer, Grain boundary complexion transitions, *Annu. Rev. Mater. Res.* **50**, 465 (2020).
- [23] T. Meiners, J. M. Duarte, G. Richter, G. Dehm, and C. H. Liebscher, Tantalum and zirconium induced structural transitions at complex [111] tilt grain boundaries in copper, *Acta Mater.* **190**, 93 (2020).
- [24] L. Langenohl, T. Brink, G. Richter, G. Dehm, and C. H. Liebscher, Atomic-resolution observations of silver segregation in a [111] tilt grain boundary in copper, *Phys. Rev. B* **107**, 134112 (2023).
- [25] S. Plimpton, Fast parallel algorithms for short-range molecular dynamics, *J. Comp. Phys.* **117**, 1 (1995).
- [26] A. P. Thompson, H. M. Aktulga, R. Berger, D. S. Bolintineanu, W. M. Brown, P. S. Crozier, P. J. in 't Veld, A. Kohlmeyer, S. G. Moore, T. D. Nguyen, R. Shan, M. J. Stevens, J. Tranchida, C. Trott, and S. J. Plimpton, LAMMPS - a flexible simulation tool for particle-based materials modeling at the atomic, meso, and continuum scales, *Comput. Phys. Commun.* **271**, 108171 (2022), <https://lammmps.org/>.
- [27] Y. Mishin, M. J. Mehl, D. A. Papaconstantopoulos, A. F. Voter, and J. D. Kress, Structural stability and lattice defects in copper: Ab initio, tight-binding, and embedded-atom calculations, *Phys. Rev. B* **63**, 224106 (2001).
- [28] Y. Mishin, D. Farkas, M. J. Mehl, and D. A. Papaconstantopoulos, Interatomic potentials for monoatomic metals from experimental data and ab initio calculations, *Phys. Rev. B* **59**, 3393 (1999).
- [29] P. L. Williams, Y. Mishin, and J. C. Hamilton, An embedded-atom potential for the Cu–Ag system, *Modell. Simul. Mater. Sci. Eng.* **14**, 817 (2006).
- [30] R. Hadian, B. Grabowski, and J. Neugebauer, GB code: A grain boundary generation code, *J. Open Source Softw.* **3**, 900 (2018).
- [31] A. Stukowski, Visualization and analysis of atomistic simulation data with OVITO – the Open Visualization Tool, *Modell. Simul. Mater. Sci. Eng.* **18**, 015012 (2010), <https://ovito.org/>.
- [32] P. M. Larsen, S. Schmidt, and J. Schiøtz, Robust structural identification via polyhedral template matching, *Modell. Simul. Mater. Sci. Eng.* **24**, 055007 (2016).
- [33] T. Brink, L. Langenohl, S. Pemma, C. H. Liebscher, and G. Dehm, *Datasets for “Stable nanofacets in [111] tilt grain boundaries of face-centered cubic metals”*, Zenodo (2024).
- [34] J. P. Hirth and J. Lothe, *Theory of Dislocations*, 2nd ed. (Krieger Publishing Company, Malabar, Florida, USA, 1992).
- [35] R. C. Pond, TEM studies of line defects in interfaces, *Ultramicroscopy* **30**, 1 (1989).
- [36] W. T. Read and W. Shockley, Dislocation models of crystal grain boundaries, *Phys. Rev.* **78**, 275 (1950).
- [37] T. Frolov, D. L. Medlin, and M. Asta, Dislocation content of grain boundary phase junctions and its relation to grain boundary excess properties, *Phys. Rev. B* **103**, 184108 (2021).
- [38] See Supplemental Material at [link to be inserted by publisher] for supplemental data and analyses.
- [39] J. D. Eshelby, W. T. Read, and W. Shockley, Anisotropic elasticity with applications to dislocation theory, *Acta Metall.* **1**, 251 (1953).

- [40] A. J. E. Foreman, Dislocation energies in anisotropic crystals, *Acta Metall.* **3**, 322 (1955).
- [41] A. N. Stroh, Dislocations and cracks in anisotropic elasticity, *Philos. Mag. A* **3**, 625 (1958).
- [42] I. S. Winter, R. E. Rudd, T. Opperstrup, and T. Frolov, Nucleation of grain boundary phases, *Phys. Rev. Lett.* **128**, 035701 (2022).
- [43] F. R. N. Nabarro, Mathematical theory of stationary dislocations, *Adv. Phys.* **1**, 269 (1952).
- [44] P. Lejček, *Grain Boundary Segregation in Metals* (Springer, Berlin, Germany, 2010).
- [45] O. L. Alerhand, D. Vanderbilt, R. D. Meade, and J. D. Joannopoulos, Spontaneous formation of stress domains on crystal surfaces, *Phys. Rev. Lett.* **61**, 1973 (1988).
- [46] It is $\frac{d}{dL} k' L^{-1} \ln(L/\delta_0) = k' L^{-2} (1 - \ln L/\delta_0)$. The function's single extremum is thus at $L = e\delta_0$, where its second derivative $\frac{d^2}{dL^2} k' L^{-1} \ln(L/\delta_0) = k' L^{-3} (2 \ln L/\delta_0 - 3)$ is positive (condition for minimum) only for $k' = k_1 b^2 + k_2 f b - k_3 f^2 < 0$.
- [47] T. Frolov and Y. Mishin, Thermodynamics of coherent interfaces under mechanical stresses. I. Theory, *Phys. Rev. B* **85**, 224106 (2012).
- [48] T. Frolov and Y. Mishin, Thermodynamics of coherent interfaces under mechanical stresses. II. Application to atomistic simulation of grain boundaries, *Phys. Rev. B* **85**, 224107 (2012).
- [49] T. Mura, *Micromechanics of Defects in Solids*, 2nd ed. (Kluwer Academic Publishers, Dordrecht, Netherlands, 1987).
- [50] It should be noted that the excess stresses in Eq. 7 would in principle also have to be rotated by $\pm\phi$. However, the stresses are affected by the somewhat complex boundary conditions for which they are defined [48]: The direction normal to the GB plane has open boundary conditions, while the other directions are fixed/periodic. The rotated stress tensor would thus have to be calculated with an inclined GB in a periodic box, which is not possible without introducing additional defects. We therefore settle here for a qualitative argument.
- [51] V. I. Marchenko, Possible structures and phase transitions on the surface of crystals, *JETP Lett.* **33**, 381 (1981).
- [52] J. B. Hannon, F.-J. Meyer zu Heringdorf, J. Tersoff, and R. M. Tromp, Phase coexistence during surface phase transitions, *Phys. Rev. Lett.* **86**, 4871 (2001).
- [53] H. J. W. Zandvliet, R. van Gastel, O. Gurlu, and B. Poelsema, Coexistence of (2×1) and $c(4 \times 2)$ phases on Ge(001), *Phys. Lett. A* **326**, 457 (2004).
- [54] D. Hull and D. J. Bacon, *Introduction to Dislocations*, 5th ed. (Elsevier Butterworth-Heinemann, Oxford, UK, 2011).
- [55] J. Han, S. L. Thomas, and D. J. Srolovitz, Grain-boundary kinetics: A unified approach, *Prog. Mater. Sci.* **98**, 386 (2018).
- [56] S. Pemma, R. Janisch, G. Dehm, and T. Brink, Effect of the atomic structure of complexions on the active disconnection mode during shear-coupled grain boundary motion, [arXiv:2305.10275 \[cond-mat.mtrl-sci\]](https://arxiv.org/abs/2305.10275) (2024).